Ocean Engineering 301 (2024) 117527

Contents lists available at ScienceDirect

Ocean Engineering

journal homepage: www.elsevier.com/locate/oceaneng

Research paper

Flow three-dimensionality of wavy elliptic cylinder: vortex shedding bifurcation

Xiaoyu Shi [a], Md. Mahbub Alam [a,*], Hongjun Zhu [b], Chunning Ji [c], Honglei Bai [d], Mohsen Sharifpur [e]

[a] Center for Turbulence Control, Harbin Institute of Technology (Shenzhen), Shenzhen, 518055, China
[b] State Key Laboratory of Oil and Gas Reservoir Geology and Exploitation, Southwest Petroleum University, Chengdu, 610500, China
[c] State Key Laboratory of Hydraulic Engineering Intelligent Construction and Operation, Tianjin University, Tianjin 300350, China
[d] School of Aeronautics and Astronautics, Sun Yat-Sen University, Shenzhen Campus (Shenzhen Campus of Sun Yat-Sen University), Shenzhen, 518107, China
[e] School of Mechanical, Industrial and Aeronautical Engineering, The University of the Witwatersrand, Private Bag 3, Wits 2050, South Africa

ARTICLE INFO

Keywords:
Three-dimensionality
Wavy elliptic cylinder
Bifurcation flow

ABSTRACT

The three-dimensional flow of a wavy elliptic cylinder and its wake are investigated for wavelength (λ) to hydraulic diameter (D_m) ratio λ/D_m = 3.43, 4.58, and 6.01. The study aims to gain insights into flow separation, flow dynamics, and three-dimensional flow topologies for the selected wavelengths. Three-dimensional flow structures are visualized through time-averaged streamlines with critical point theory. The results for λ/D_m = 3.43 show spiral flow directed from the node to the saddle, counter-rotating vortices, and a wavy vortex structure. On the contrary, the flows for λ/D_m = 4.58 and 6.01 respectively undergo bifurcation in stable recirculation and vortex shedding on a half-span of the cylinder wavelength. The bifurcation results in a spiral flow toward the saddle and the other spiral flow toward the node. The bifurcations of recirculation and vortex shedding are revealed for the first time. The findings contribute to an improved understanding of the insight into intricate flow physics around wavy elliptic cylinders.

1. Introduction

Flow past a cylinder has garnered significant attention because of its prevalence in engineering applications and nature. Generally, the cross-section of a structure may be of a circular or a square shape. The circular-sectioned or square-sectioned structures have thus been extensively studied as the fundamental models, either numerically (Bai and Alam, 2018; Abdelhamid et al., 2021; Rastan et al., 2021, 2022; Chen et al., 2022, 2023) or experimentally (Alam et al., 2003, 2016; Alam, 2014; Wang et al., 2017). Please refer to Williamson (1996), Derakhshandeh and Alam (2019), Alam (2023a, 2023b, 2022), and Mondal and Alam (2023) for comprehensive recent reviews of flow around circular, square, and rectangular cylinders. Furthermore, considerable focus has also been given to slender cylinders with an elliptic cross-section (Paul et al., 2016; Shi et al., 2020). Additionally, introducing a sinusoidal spanwise waveform may appreciably modify the flow topology and reduce the drag and lift forces on the structure (Ahmed and Bays-Muchmore, 1992; Bearman and Owen, 1998; Lam and Lin, 2008; Lin et al., 2016; Assi and Bearman, 2018; Shi et al., 2023). These modified structures, known as wavy cylinders, are considered an effective approach to controlling the flow, reducing fluid forces, and suppressing flow-induced vibrations (Beem and Triantafyllou, 2015; Lin et al., 2016; Assi and Bearman, 2018). For comprehensive effects of spanwise waviness on elliptic, circular, and square cylinders at different Reynolds numbers, refer to the study by Shi et al. (2023).

The wake of and fluid forces on wavy elliptic cylinders have gained considerable focus from researchers (Wang and Liu, 2016; Jie and Liu, 2017; Rinehart et al., 2017; Assi and Bearman, 2018; Shi et al., 2023). A harbor seal whisker is generally elliptic, having a wavy surface (of wavelength λ) along the whisker axis (Fig. 1). Compared to a straight cylinder, a wavy elliptic cylinder can modify the vortex shedding, making the flow incoherent, and elongate the vortex formation length, reducing the fluid force. The cross-sectional aspect ratio (AR) is specified as the ratio of the minor and major axes. On the other hand, the ratio of the surface wavelength λ and mean minor diameter $D_m = (D_n + D_s)/2$ defines the normalized wavelength λ/D_m, with D_n and D_s being the minor-axis diameters at the node and saddle sections, respectively. Shi et al. (2023) proposed a simplified seal-whisker-based cylinder model on

* Corresponding author.
E-mail addresses: alamm28@yahoo.com, alam@hit.edu.cn (Md.M. Alam).

https://doi.org/10.1016/j.oceaneng.2024.117527
Received 2 December 2023; Received in revised form 27 February 2024; Accepted 13 March 2024
Available online 26 March 2024
0029-8018/© 2024 Elsevier Ltd. All rights reserved.

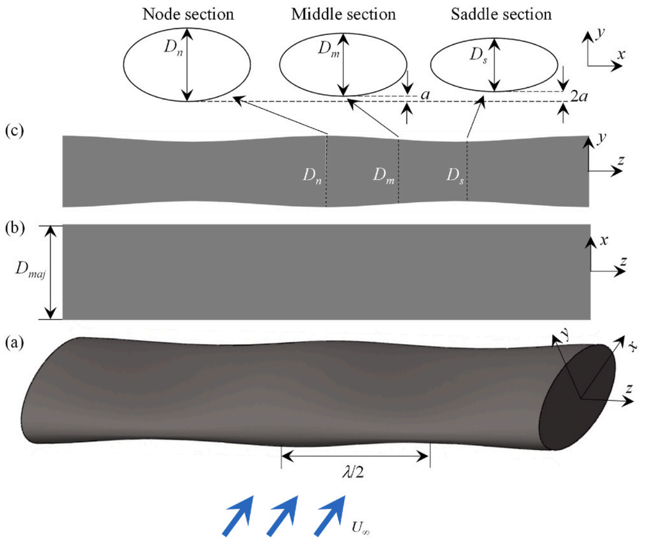

Fig. 1. (a) Schematic diagram of the wavy elliptic cylinder (WEC) and symbol designation. (b) Top view. (c) Front view.

which the wavy surface is generated from a sinusoidal variation of the minor axis, keeping the major axis constant. The amplitude of the surface wave was $a/D_m = 0.048$ while the λ/D_m was varied from 0.43 to 8.59. They investigated the flow dependence on λ/D_m at $Re = 100$ based on D_m and identified five flow patterns (I – V). Two-dimensional and alternate vortex shedding characterizes pattern I ($\lambda/D_m < 2.58$). The flow is three-dimensional in pattern II ($2.58 < \lambda/D_m < 4.44$), with alternate vortex shedding. Pattern III ($4.44 < \lambda/D_m < 5.01$) represents steady flow, featuring minimum drag force. Pattern IV ($5.01 < \lambda/D_m < 6.40$) offers zero fluctuating lift force because alternate vortex shedding over one-half wavelength is antiphased with the shedding over the other half wavelength. When $\lambda/D_m > 6.40$, pattern V appears, characterized by a highly three-dimensional wake.

Existing studies have primarily focused on classifying flow patterns, measuring fluid forces, and suppressing flow-induced vibration (FIV) for cylinders with circular, square, or elliptic sections (Qin et al., 2017, 2019; Bhatt and Alam, 2018; Alam, 2021; Thompson et al., 2014). Recent advancements in computer hardware technology and computational fluid dynamics techniques have made it feasible to numerically explore three-dimensional complex flow interactions. In this context, the critical-point theory has emerged as a useful tool for describing complex flows around two-dimensional circular or square cylinders (Huang et al., 2006, 2010; Cao et al., 2022), turbulent channel flow (Stroh et al., 2016; Castro et al., 2021), low Reynolds number flows around surface-mounted cubes (Liakos and Malamataris, 2014, 2016), and flows around hemisphere cylinders (Le Clainche et al., 2016). However, limited work has been devoted to the three-dimensional topology of flow around wavy cylinders, including those with circular, square, or elliptic cross-sections. Castro et al. (2021) focused on clarifying the location of critical points by investigating the velocity field at cross-planes for all the critical points. On the other hand, Cao et al. (2022) identified the critical points in terms of skin friction on the wall and surfaces of a finite square cylinder. While the critical-point theory has been successfully used in various flow scenarios, its application to understanding the three-dimensional topology of flow around wavy cylinders remains limited. Further investigation in this area is necessary to comprehensively understand the flow characteristics and interactions associated with wavy cylinder geometries.

However, there is a need to investigate the behavior of the three-dimensional topology of flow around a wavy elliptic cylinder. Shi et al. (2023) primarily concentrated on vortical structures, Strouhal numbers, wake recirculation, and fluid forces associated with different flow patterns. However, they did not address the three-dimensional flow topologies and bifurcation involved in vortex shedding. Moreover, understanding the relationship between the three-dimensional topology and fluid force reduction is crucial. To gain further insight, the present study extends the work by Shi et al. (2023), exploring the three-dimensional flow topology in the wavy-elliptic cylinder wake, vortex shedding bifurcation, and their connections to fluid force. The objective of this work is to examine the three-dimensional topologies of a wavy elliptic cylinder using critical point theory at $Re = 100$. The wavy elliptic cylinder utilized is the same as the one employed by Shi et al. (2023). We home in on the understanding of the flow topologies and the flow evolutions. The study specifically focuses on three selected λ/D_m values corresponding to flow pattern II ($\lambda/D_m = 3.43$), III ($\lambda/D_m = 4.58$), and IV ($\lambda/D_m = 6.01$) as defined in Shi et al. (2023). The waviness of the wavy elliptic cylinder is fixed at $a/D_m = 0.048$.

2. Problem and numerical details

2.1. Whisker model

A schematic of the whisker model is shown in Fig. 1, defining the different parameters. The wavy surface is generated from a sinusoidal variation of the minor axis (D_{min}) along the spanwise direction (z) of the elliptic cross-section while the major axis (D_{maj}) of the elliptical cross-section remains constant. The mathematical expression for D_{min} is:

$$D_{min} = D_m + 2a\sin(2\pi z/\lambda) \tag{1}$$

where D_m represents the average minor axis, λ denotes the wavelength and a stands for the wave amplitude (or waviness). Here, the maximum and minimum minor axes are denoted by D_n and D_s, respectively. The corresponding cross-sections perpendicular to the cylinder axis are referred to as the node section and saddle sections, respectively. The mean minor axis at the mid-section is defined as $D_m = (D_n + D_s)/2$. Three representative wavelengths of the wavy elliptic cylinder are investigated: $\lambda/D_m = 3.43$, 4.58, and 6.01 corresponding to flow patterns II, III, and IV, respectively, as defined by Shi et al. (2023). Here, we set a constant wave amplitude of $a/D_m = 0.048$, which corresponds to cross-sectional aspect ratio $AR = (D_{min}/D_{maj}) = 0.55$, 0.5, and 0.45 at the node, middle, and saddle sections, respectively.

2.2. Computational domain and grids

The wavy elliptic cylinder is positioned symmetrically ($y = 0$) in the computational domain (Fig. 2a). All the distances are given in terms of D_m. The distances of the inlet and outlet boundaries from the cylinder axis ($x = 0$) are $20D_m$ and $40D_m$, respectively, while the lateral distance between the two side boundaries is $40D_m$. The spanwise size (z) of the cylinder is 2λ, representing the distance between the upper and lower boundaries. The computational domain is large enough, giving a blockage ratio of 2.5% only (Zheng and Alam, 2017, 2019). The cartesian coordinate system is employed, with the origin at the cylinder center. The x-axis is the streamwise flow direction while the y-axis is the cross-stream flow direction. The cylinder axis corresponds to the z-axis, with $z = 0$ at the lower boundary (Fig. 2a).

Quadrilateral grids are generated throughout the entire computational domain. Within a $5D_m$ circle surrounding the wavy elliptic cylinder (Fig. 2b), relatively fine grids are created. Along the circumference of the cylinder, a total of 120 grids are allocated uniformly. For $Re = 100$, the first grid height in the radial direction is set at $0.01D_m$. The distance between the adjacent grids is $0.03D_m$ in the spanwise direction. The number of grids along the cylinder axis varies depending on λ/D_m: 112, 148, and 194 grid layers for $\lambda/D_m = 3.43$, 4.58, and 6.01, respectively. The computational domain has approximately 3.2×10^6, 4.4×10^6, and 7.1×10^6 grids for $\lambda/D_m = 3.43$, 4.58, and 6.01, respectively. For $Re = 300$, a finer mesh resolution is employed for $\lambda/D_m = 6.01$. The

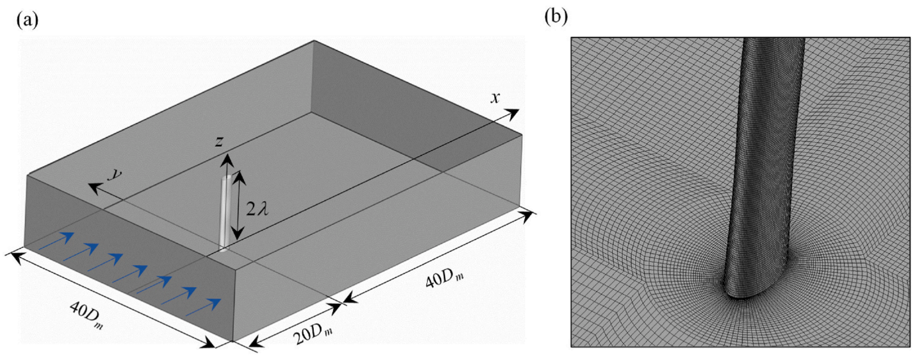

Fig. 2. (a) Computational domain and (b) mesh detail.

distance between the first grid and the cylinder surface is reduced to $0.005D_m$ while the grid resolution in the spanwise direction is $0.02D_m$. The total grid number is 1.0×10^7.

2.3. Governing equations

Three-dimensional simulations are conducted using ANSYS Fluent, using the finite-volume method. The governing equations for fluid flow in the Cartesian coordinate system can be presented as follows.

Continuity equation

$$\frac{\partial u^*}{\partial x^*}+\frac{\partial v^*}{\partial y^*}+\frac{\partial w^*}{\partial z^*}=0, \tag{2}$$

momentum equations

$$\frac{\partial u^*}{\partial t^*}+u^*\frac{\partial u^*}{\partial x^*}+v^*\frac{\partial u^*}{\partial y^*}+w^*\frac{\partial u^*}{\partial z^*}=-\frac{\partial p^*}{\partial x^*}+\frac{1}{Re}\left(\frac{\partial^2 u^*}{\partial x^{*2}}+\frac{\partial^2 u^*}{\partial y^{*2}}+\frac{\partial^2 u^*}{\partial z^{*2}}\right), \tag{3}$$

$$\frac{\partial v^*}{\partial t^*}+u^*\frac{\partial v^*}{\partial x^*}+v^*\frac{\partial v^*}{\partial y^*}+w^*\frac{\partial v^*}{\partial z^*}=-\frac{\partial p^*}{\partial y^*}+\frac{1}{Re}\left(\frac{\partial^2 v^*}{\partial x^{*2}}+\frac{\partial^2 v^*}{\partial y^{*2}}+\frac{\partial^2 v^*}{\partial z^{*2}}\right), \tag{4}$$

$$\frac{\partial w^*}{\partial t^*}+u^*\frac{\partial w^*}{\partial x^*}+v^*\frac{\partial w^*}{\partial y^*}+w^*\frac{\partial w^*}{\partial z^*}=-\frac{\partial p^*}{\partial z^*}+\frac{1}{Re}\left(\frac{\partial^2 w^*}{\partial x^{*2}}+\frac{\partial^2 w^*}{\partial y^{*2}}+\frac{\partial^2 w^*}{\partial z^{*2}}\right), \text{ and} \tag{5}$$

where u^* $(=u/U_\infty)$, v^* $(=v/U_\infty)$ and w^* $(=w/U_\infty)$ are dimensionless flow velocities in the x-, y- and z-directions, respectively, t^* $(=tU_\infty/D_m)$ is the dimensionless time, p^* $(=p/\rho U_\infty^2)$ is the dimensionless pressure, x^* $(=x/D_m)$, y^* $(=y/D_m)$ and z^* $(=z/D_m)$ are the streamwise, cross-stream, and spanwise coordinate axes, and Re $(=\rho D_m U_\infty/\mu)$ is the Reynolds number. Here, t, ρ, μ, p, and U_∞ are the time, fluid density, fluid viscosity, pressure, and freestream velocity, respectively.

2.4. Boundary conditions

The symmetry boundary condition is imposed on the lateral sides ($y = \pm 20D_m$): $v^*=0$, $\partial u^*/\partial y^*=0$, and $\partial w^*/\partial y^*=0$ while the top and bottom sides ($z=0, 2\lambda$) are given the periodic boundary condition. The cylinder surface is set with $u^*=v^*=w^*=0$. The flow at the inlet is uniform (i.e. $u^*=1$, $v^*=w^*=0$) while that at the outlet is conditioned with $\partial u^*/\partial x^*=0$, $\partial v^*/\partial x^*=0$, $\partial w^*/\partial x^*=0$. The spatial discretization for pressure and momentum employs the second-order implicit scheme for pressure and the upwind differencing scheme for momentum. For the temporal discretization, the second-order implicit scheme is used. The pressure-velocity coupling in the governing equation is handled using the Pressure-Implicit with Splitting of Operators (PISO) method. The dimensionless time steps are set as $\Delta t^*=0.025$ and 0.003 for $Re=100$ and 300, respectively. To ensure statistically independent results, we recorded data for over 50 cycles of vortex shedding.

2.5. Grid and time-step independence tests

Before performing the extensive simulations, grid and time-step independence tests are meticulously conducted to ensure the reliability and accuracy of the simulation outcomes. Initially, straight elliptic cylinders with aspect ratios (AR) of 0.5 and 1.0 are selected for the grid independence test at $Re=100$. The results, encapsulated in Table 1, summarize the key output parameters: time-mean drag coefficient ($\overline{C}_D$), fluctuating lift coefficient (C'_L), and Strouhal number (St) for three different mesh systems differentiated by the uniformity of nodes generated along the circumferential (N_c) and spanwise (N_z) directions. The data reveals that doubling N_z from 63 to 126 leads to a decrease in $\overline{C}_D$ and an increase in C'_L. The change in C'_L is more pronounced for $AR=1.0$. Additionally, increasing N_c from 120 to 160 provides nearly converged outputs, which indicates the suitability of the second mesh system (M2) for subsequent simulations.

Following the grid independence verification, time-step independence tests are performed for a straight circular cylinder (Table 2). A reduction in the time step from 0.025 to 0.0125 confirms the convergence of output parameters, with a largest deviation of 1.25% in C'_L. Based on these comprehensive tests, mesh system M2 and a time step of $t^*=0.025$ are selected for the simulations in this work.

2.6. Validation

To validate the numerical scheme, flow is simulated for a straight circular cylinder, and the results are compared with those in the literature (Table 3). The present study's results generally agree with the published data. The value of $\overline{C}_D$ is 1.384 in the present study, very close to that (1.389) reported by Kumar et al. (2018). The deviation in $\overline{C}_D$ is less than 5% when compared to other studies (e.g. He et al., 2000; Zhang et al., 1995; Lam and Lin, 2009; Alam, 2023a). The deviation in C'_L between the present (0.236) and Lam and Lin's (2009) (0.234) works is very small (0.85%) while that between the present (0.236) and others is less than 6%. On the other hand, a maximum deviation in St of less than 3.05% is observed between the present and other studies in Table 3. These comparisons indicate that the present results are in good agreement with those reported in the literature.

Table 1
Grid independence test for a straight elliptic cylinder with $AR=0.5$ and 1.0 at $Re=100$.

	$N_c \times N_z$	$AR=0.5$			$AR=1.0$		
		$\overline{C}_D$	C'_L	St	$\overline{C}_D$	C'_L	St
M1	120 × 63	1.080	0.048	0.148	1.387	0.222	0.170
M2	120 × 126	1.076	0.050	0.148	1.384	0.236	0.169
M3	160 × 126	1.076	0.051	0.148	1.384	0.237	0.169

Table 2
Time step independence test for a straight circular cylinder at $Re = 100$.

Mesh	Time step (t^*)	$\overline{C}_D$	$C_L^{'}$	St
M1	0.0125	1.385	0.240	0.170
	0.025	1.384	0.237	0.170
	0.050	1.383	0.232	0.170
M2	0.0125	1.384	0.239	0.169
	0.025	1.384	0.236	0.169
	0.050	1.382	0.230	0.169
M3	0.0125	1.385	0.241	0.169
	0.025	1.384	0.237	0.169
	0.050	1.383	0.230	0.169

Table 3
Comparison of results between the present and previous studies for a straight circular cylinder. ($Re = 100$).

Studies	$\overline{C}_D$	$C_L^{'}$	St
Present	1.384	0.236	0.169
Alam (2023a), *Num.*	1.318	0.226	0.164
Abdelhamid et al. (2021), *Num.*	1.37	0.22	0.167
Kumar et al. (2018), *Num.*	1.388	0.251	0.167
Lam and Lin (2009), *Num.*	1.34	0.234	0.164
Kang (2003), *Num.*	1.33	–	0.165
He et al. (2000), *Num.*	1.35	–	0.167
Zhang et al. (1995), *Num.*	1.421	0.247	0.172
Williamson (1989), *Exp.*	–	–	0.164

3. Results and discussion

Three different wavelengths ($\lambda/D_m = 3.43$, 4.58, and 6.01) are chosen for the investigation, and the corresponding vortex shedding structures are displayed in Fig. 3. Both global (Fig. 3a, b, c) and sectional (Fig. 3d, e, f) views of vortex shedding structures are provided for the three λ/D_m values. The global views of the vortex structures are represented by the iso-surface of spanwise vorticity (ω_z^*) = 0.1 and colored by the streamwise vorticity ($\omega_z^* = \pm 0.1$). Here, we provide a brief overview of the flow topologies for the three wavelengths. Flow pattern at $\lambda/D_m = 3.43$ is characterized by wavy spanwise vortices and a pair of counter-rotating streamwise vortices (Fig. 3 a, d). The flow pattern at $\lambda/D_m = 4.58$ represents a steady flow pattern where alternate vortex shedding is fully suppressed (Fig. 3b–e). In this case, no periodic vortex shedding occurs. Flow pattern at $\lambda/D_m = 6.01$ exhibits both large-scale streamwise and disconnected spanwise vortices (Fig. 3c–f). The spanwise vortex shedding is synchronized over a one-half span (0.5λ) of the cylinder, being antiphased with that over the other half span. By examining time-mean streamline traces, a better insight into the flow dynamics can be obtained, particularly in view of the flow separation and flow physics.

3.1. Flow separation and wake recirculation

It is widely recognized that flow separation around a straight circular or elliptic cylinder is dynamic and oscillatory over a segment of the curved surface because of periodic vortex shedding from the cylinder. Particularly, in the case of a wavy cylinder, the wavelength plays a crucial role in modulating the location of flow separation. It is worth investigating the surface flow separation and the accompanying wake circulation bubble for a wavy cylinder. Understanding the behavior of flow separation and the formation of wake bubbles can provide insights into the complex flow physics and shed light on the mechanisms behind the interaction between the wavy cylinder surface and the flow field.

Fig. 4 presents a perspective view of the averaged streamlines on the axis-symmetric plane ($y = 0$) along with the same on the xy-plane at the saddle (S) and node (N) sections, for $\lambda/D_m = 3.43$, 4.58, and $\lambda/D_m = 6.01$. The streamlines on the left ($y < 0$) and right ($y > 0$) sides are colored black (solid) and blue (dashed), respectively. It is observed that the streamlines on the cylinder surface are slightly bent toward the saddle, which is more perspicuous just before the separation line (Fig. 4). It implies that the flow close to the cylinder surface travels from the node to the saddle. As a result, the flow separation at the node occurs ahead of that at the saddle. Conversely, for shorter wavelengths ($\lambda/D_m <$ 2.58, as noted by Shi et al., 2023), the saddle section has an earlier flow separation than the node section. Correspondingly, the flow close to the cylinder surface shifts sideways from the saddle plane to the node plane. Thus, it can be concluded that the direction of the flow from the saddle to the node or vice versa steers the flow separation trajectory along the cylinder span. The flow heading for the node plane brings in a delayed flow separation at the node, and vice versa. The flow separations at the node and saddle sections are respectively found to be 146.6° and 157.0° for $\lambda/D_m = 3.43$, 141.8° and 157.0° for $\lambda/D_m = 4.58$, and 143.0° and 158.4° for $\lambda/D_m = 6.01$.

The recirculation bubble behind the cylinder exhibits a streamwise extent starting from the flow separation line on the cylinder surface. The size of the recirculation bubble varies between the node and saddle sections, as marked by the red dashed line. For the case of $\lambda/D_m = 3.43$ (Fig. 4a), the streamwise size of the recirculation bubble is smaller at the saddle than at the node, which is associated with the three-dimensional undulation of the cylinder, hence the flow. The bubble size at the node

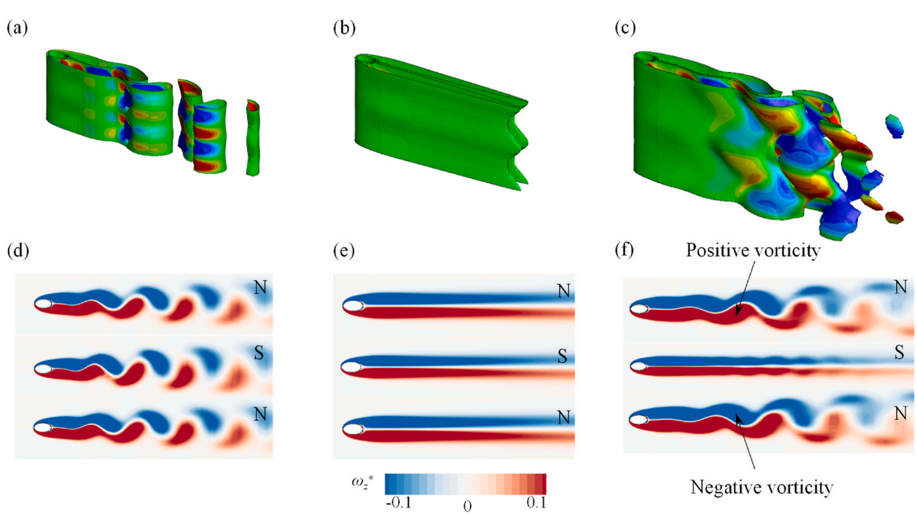

Fig. 3. Instantaneous vortex structures for (a, d) $\lambda/D_m = 3.43$, (b, e) $\lambda/D_m = 4.58$, and (c, f) $\lambda/D_m = 6.01$. The upper row displays the spanwise vorticity (ω_z*) iso-surface of ω_z* = 0.1 (colored by streamwise vorticity ω_x*). The lower row provides ω_z* contours at the node and saddle sections. Here, $Re = 100$.

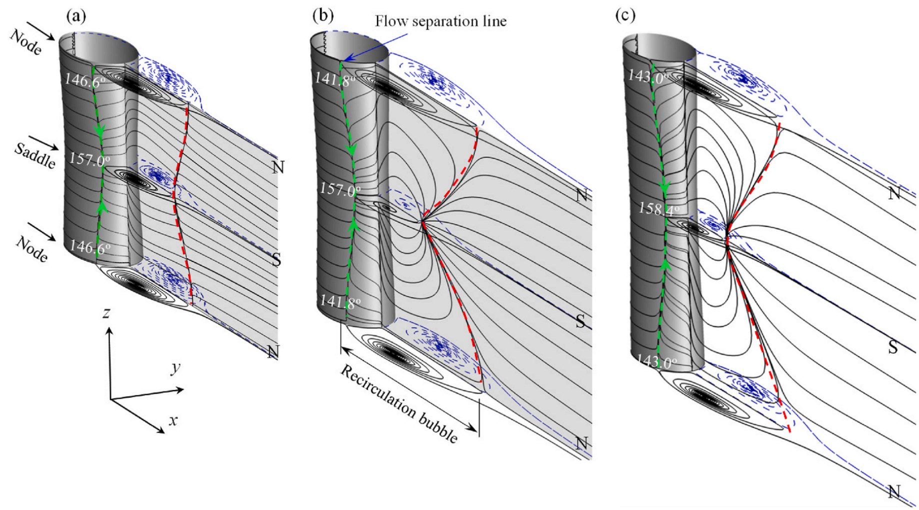

Fig. 4. Distributions of time-mean streamlines on the *xy*-plane (saddle and node sections denoted by 'S' and 'N', respectively) and on the *xz*-plane (at $y = 0$) for (a) $\lambda/D_m = 3.43$, (b) $\lambda/D_m = 4.58$ and (c) $\lambda/D_m = 6.01$. The red dashed line denotes the streamwise extent of the recirculation bubble, and the green dashed lines on the cylinder surface are flow separation lines. The given values of separation angles are at the node and saddle sections. Black solid lines refer to the streamline on the left side ($y < 0$) while the blue dashed lines stand for streamlines on the right side ($y > 0$). Here, $Re = 100$.

plane differs from that at the saddle plane by a small margin. In contrast, for $\lambda/D_m = 4.58$ and 6.01, there is a significant variation in the sizes of the recirculation bubbles along the spanwise direction, with the shortest size observed at the saddle plane (Fig. 3b, c). This dramatic difference in the sizes of the recirculation bubbled is auspicious for the formation of large-scale streamwise vortices along the span. The distinct variations in the recirculation bubble sizes provide insight into the flow dynamics.

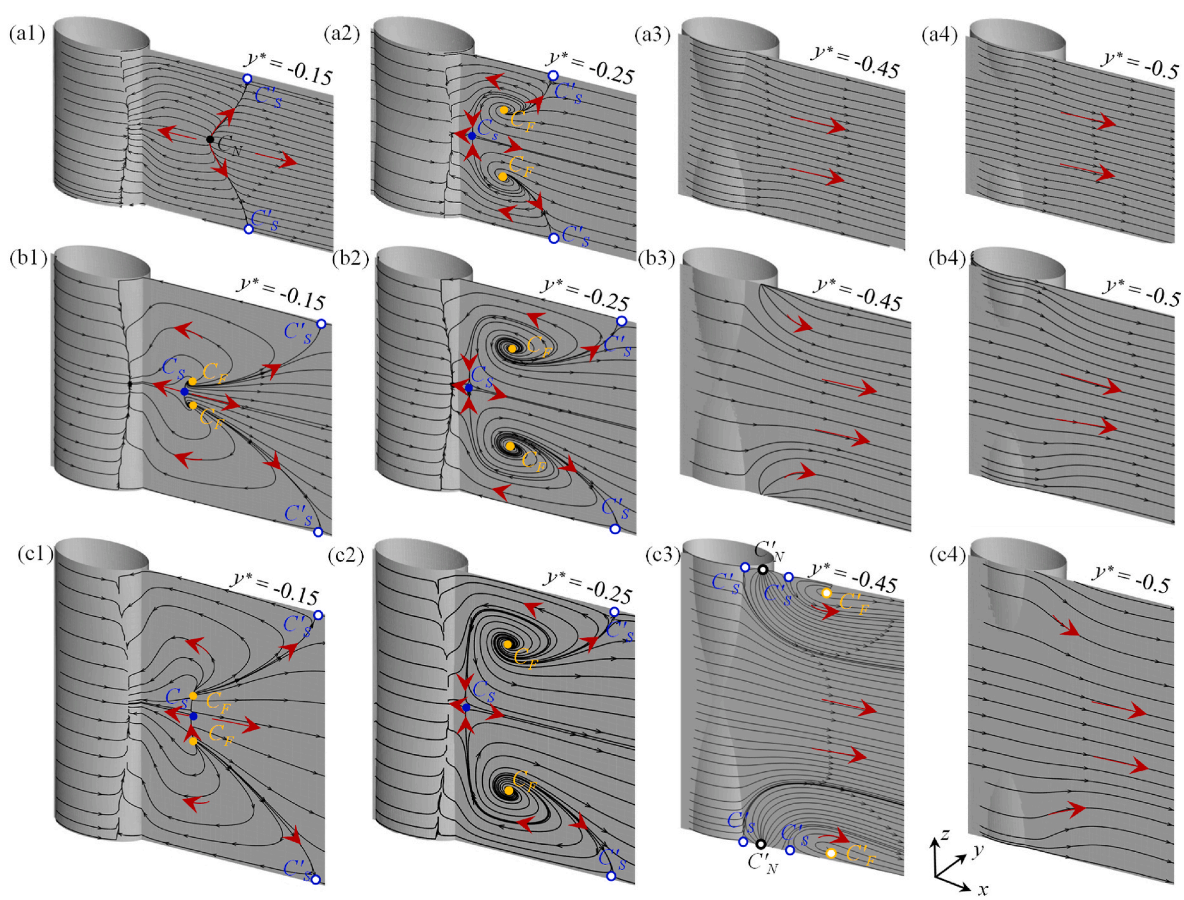

Fig. 5. Distributions of time-mean streamlines on the *xz*-plane at $y^* = -0.15$ (a1 – c1), -0.25 (a2 – c2), -0.45 (a3 – c3), and -0.5 (a4 – c4) for $\lambda/D_m = 3.43$ (flow pattern II, a1 – a4), 4.58 (III, b1 – b4), and 6.01 (IV, c1 – c4). The marks ●, ●, and ● denote critical node, saddle, and focus points; ○ and ○ refer to half critical saddle and focus points, respectively. Here, $Re = 100$.

3.2. Three-dimensional flow topology

Figs. 5 and 6 show time-averaged streamline traces on the *xz*- and *yz*-planes. Four *xz*-planes at $y^* = -0.15$, -0.25, -0.45, and -0.5 (Fig. 5) and four *yz*-planes at $x^* = 1.0$, 1.75, 2.0, and 3.0 (Fig. 6) are considered. The critical points, including saddle (C_S), node (C_N), and focus (C_F), are marked in each plane, based on the topological behavior of the streamlines. The saddle point C_S can be defined as the point where there are two inward streamlines and two outward streamlines from C_S, while the node point C_N is a singular point where all the streamlines approaching it share one tangent or have different slopes (Délery, 2001). The focus (C_F) is characterized by the spiral flow, from which a set of streamlines originates or at which a set of streamlines ends. Note that our discussion on the topology of the streamlines is confined within one spanwise wavelength, and thus the critical points identified on the boundaries of the confinement (i.e., the node plane of the cylinder) are designated as half critical points, distinguished by the superscript '''. As the focus belongs to the nodal points, the relationship between the critical point numbers is $(\sum C_{N\ or\ F} + \frac{1}{2}\sum C^{'}_{N\ or\ F}) - (\sum C_S + \frac{1}{2}\sum C^{'}_S) = 0$ (Hunt et al., 1978), holding for each plane.

For the cylinder with $\lambda/D_m = 3.43$, the streamline traces on the *xz*-plane at $y^* = -0.15$ (Fig. 5a1) behave in a wavy fashion, with one C_N and two C'_S. The flow passing through the middle plane goes towards the two node boundaries in the recirculation bubble. However, two additional C_F connecting C_S and C'_S can be detected in the plane at $y^* = -0.25$ (Fig. 5a2). The flows from these two C_F are spirally directed toward the nodes and saddles, generating one C_S at the saddle plane and two C'_S at the node planes. The C_F comes into being because the recirculation bubble core is not parallel to the cylinder axis. As the inclination of the recirculation bubble core for $\lambda/D_m = 3.43$ is relatively small, C_F can only be observed at $y^* = -0.25$. There are no critical points detected for $y^* \leq -0.45$ (Fig. 5a3, a4), indicating that the lateral width of the recirculation bubble is smaller than 0.9. In the cross-stream *yz*-plane at $x^* = 1.0$ (Fig. 6a1), C_S and C_N alternately appear on the cylinder saddle plane while C'_S and C'_N occur on the upper and lower boundaries (node planes) oppositely to C_S and C_N in the saddle plane. The scenario reflects that the spiral flow is directed from the cylinder node to the saddle. At $x^* = 1.75$ (Fig. 6a2), there are five C'_S on each of the upper and lower boundaries and five C_N on the cylinder saddle plane. The second and fourth C_N from the left represent the recirculation bubble core. At $x^* = 2.0$ (Fig. 6a3), only one C_S materializes on the saddle plane and a pair of C'_F appears on each node plane. The latter is linked to the

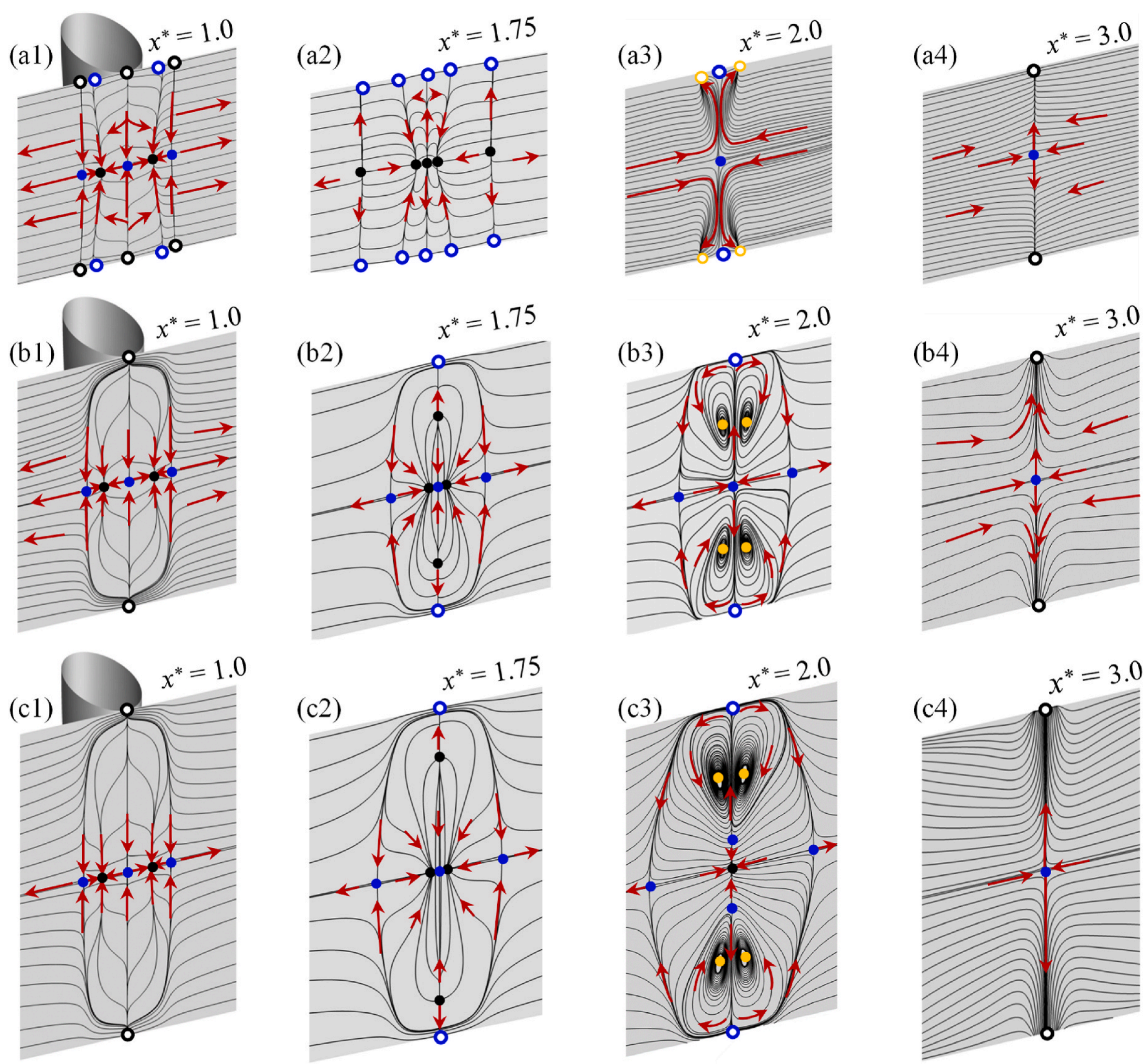

Fig. 6. Distributions of time-mean streamlines on the *yz*-plane at $x^* = 1.0$ (a1 – c1), $x^* = 2.0$ (a2 – c2), and $x^* = 3.0$ (a3 – c3) for $\lambda/D_m = 3.43$ (a1 – a3), $\lambda/D_m = 4.58$ (b1 – b3), and $\lambda/D_m = 6.01$ (c1 – c3). The marks ●, ●, and ● denote critical node, saddle, and focus points; ○, ○ and ○ refer to half critical node, saddle and focus points, respectively. Here, $Re = 100$.

recirculation bubble at the node plane, i.e. corresponding to C'_S in Fig. 5a. Now the flow in the wake centerline plane ($y^* = 0$) is from the cylinder saddle plane to the node plane. When x^* is further increased, the two C'_F is replaced by a single C'_N at $x^* = 3.0$ as $x^* = 3.0$ is beyond the recirculation bubble (Fig. 6a4).

In the cases of $\lambda/D_m = 4.58$ and 6.01, two C_F appear at $y^* = -0.15$ (Fig. 5b1, c1) and -0.25 (Fig. 5b2, c2). The two C_F move away from the saddle plane with an increase in y^* from -0.15 to -0.25 (Fig. 5b2, c2) as the streamwise position of the recirculation bubble core elongates from the cylinder saddle plane to the node plane. The streamline pattern at $y^* = -0.45$ for $\lambda/D_m = 6.01$ differs from that for $\lambda/D_m = 4.58$ (Fig. 5b3, c3), where C'_F features in the node plane for $\lambda/D_m = 6.01$. This is because of the relatively wider recirculation bubble at the node plane for $\lambda/D_m = 6.01$. The plane at $y^* = -0.45$ for $\lambda/D_m = 4.58$ is close to the flow separation on the cylinder. The critical points are, therefore, hard to define for $\lambda/D_m = 4.58$. Finally, the flow three-dimensionality weakens at $y^* = -0.5$ (Fig. 5b4, c4), as this plane is out of the recirculation bubble.

In the yz-plane, quite similar topologies emerge for $\lambda/D_m = 4.58$ and 6.01 (Fig. 6). At $x^* = 1.0$ (Fig. 6b1, c1), C_S and C_N appear alternately at the saddle plane while one C'_N is on the boundary. In the recirculation bubble, the flow spirals from the node plane to the saddle plane. This is, however, not the case at $x^* = 1.75$ (Fig. 6b2, c2), where the flow in the bubble for a small part of the cylinder span near the node heads for the node plane while the rest of the span has the flow heading for saddle plane. The scenario echoes a bifurcation in vortex shedding, which will be further discussed later. At $x^* = 2.0$ (Fig. 6b3, c3), there are four C_F points symmetrically distributed about the saddle plane and $y^* = 0$ plane, which are the signatures of the spiral flow in the recirculation bubble. The bifurcation still exists for $\lambda/D_m = 6.01$ (Fig. 6c3), moving toward the saddle plane. Combining the flow topology in xy- (Fig. 4b, c), xz- (Fig. 5b2, c2), and yz- (Fig. 6b3, c3) planes, it is understood that the streamlines spiral on both xz- and yz-planes as the recirculation core trajectory varies along the cylinder span. At $x^* = 3.0$ (Fig. 6b4, c4), the flow goes from the saddle plane to the node plane, having one C_S and two C'_S points.

To provide a deeper flow topology, the time-averaged streamlines on the orthogonal yz- ($x^* = 1.75$) and xy-planes, colored by the time-mean spanwise velocity ($\overline{w}^*$), are presented in Fig. 7 for the three distinct flow patterns. Slightly more than the upper half wavelength is displayed. The bottom xy-plane corresponds to the saddle plane, and the planes marked by '●' are the bifurcation planes. The streamlines on xy-planes display recirculation bubbles while those in yz-planes show upward or downward flow. For $\lambda/D_m = 3.43$ (Fig. 7a), the streamlines flow from the node toward the recirculation bubble cores at the saddle plane. The $\overline{w}^* \approx 0$ (green color) can be detected in the vicinity of the saddle plane. The $\overline{w}^* \approx 0$ at the arc (Fig. 7a1) on the xy-plane results from the three-dimensional spiral recirculation. The $\overline{w}^* < 0$ and $\overline{w}^* > 0$ are before and after the arc, respectively (Fig. 7a1), where the arc refers to the isoline of $\overline{w}^* \approx 0$, and the blue and red colors indicate $\overline{w}^* < 0$ and $\overline{w}^* > 0$, respectively. The selected plane at $x^* = 1.75$ crosses the isoline of $\overline{w}^* \approx 0$. In the cases of $\lambda/D_m = 4.58$ (Figs. 7b) and 6.01 (Fig. 7c), recirculation is shown for four selected xy-planes, two near the saddle and two near the bifurcation. The locations of the bifurcation are $0.30\lambda/D_m$ and $0.38\lambda/D_m$ away from the saddle plane for $\lambda/D_m = 4.58$ and 6.01, respectively. For the lower three xy-planes, the yz-plane at $x^* = 1.75$ lies upstream of the $\overline{w}^* \approx 0$ arc. The corresponding streamlines on the yz-plane are thus blue, indicating a downward flow. The streamlines near the center plane

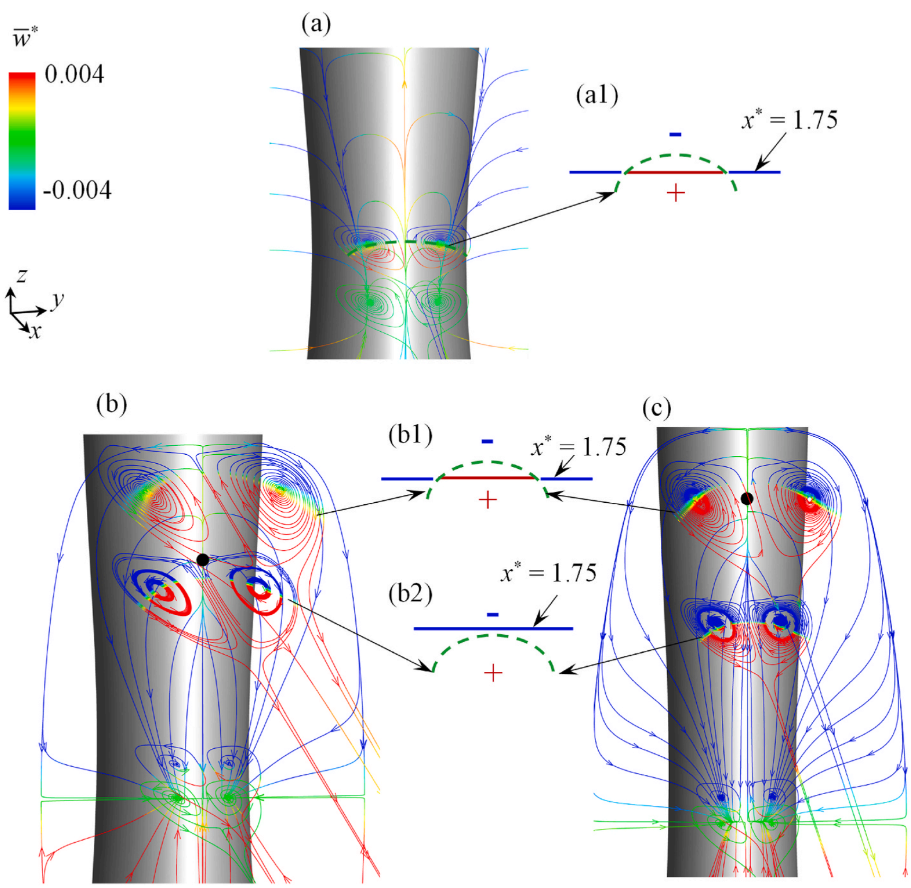

Fig. 7. Time-mean streamlines on the orthogonal yz- ($x^* = 1.75$) and xy-planes, colored by the time-mean spanwise velocity ($\overline{w}^*$) for (a) $\lambda/D_m = 3.43$, (b) $\lambda/D_m = 4.58$, and (c) $\lambda/D_m = 6.01$, The bottom xy-plane is the saddle plane, and the mark ● denotes the C_N on yz-plane. (a1, b1, b2) Sketches showing the signs of $\overline{w}^*$ on the sides of the selected yz-plane ($x^* = 1.75$). Here, $Re = 100$.

($y^* = 0$) change from blue to yellow once passing through the bifurcation plane marked by '●'. The flow above and below the bifurcation goes toward the node and saddle, respectively (Fig. 7b1, b2). Similar to $\lambda/D_m = 3.43$, the spanwise flow finally converges toward the recirculation core of the saddle plane.

Fig. 8 provides a visual representation of the instantaneous vortex shedding for the three λ/D_m values. The red arrows indicate the time-mean spiral streamlines, which give a visual representation of the flow three-dimensionality. For $\lambda/D_m = 3.43$ (Fig. 8a), the wavelength effect is evident, leading to the generation of spiral flow heading for the saddle plane. This results in the formation of counter-rotating vortices and makes the vortex structure wavy in the spanwise direction. Vortex shedding alternates between the two sides of the entire cylinder. In the case of $\lambda/D_m = 4.58$, the flow is steady, embodying a stable recirculation bubble and bifurcated spiral flows (Fig. 8b, indicated by the red dots) heading for the saddle and node planes. The flow for $\lambda/D_m = 6.01$ is characterized by the fact that the vortex shedding from a half wavelength is antiphased with that from the other (Fig. 8c). Similar to $\lambda/D_m = 4.58$ case, the flow associated with vortex shedding bifurcates (Fig. 8c, denoted by the red dots), resulting in spiral flows toward the node and saddle planes. It is worth noting that the recirculation bubble at the saddle plane is shorter than that in the node plane.

3.3. Reynolds number effect

To expand upon our understanding, we carried out further simulations for $\lambda/D_m = 6.01$ at $Re = 300$ and conducted a comparative analysis of the results between $Re = 100$ and 300 (Figs. 9 and 10). Lateral velocities (v^*) are tracked at $(x^*, y^*) = (3, 1)$ for the saddle (S1, S2), middle (M1, M2, M3, M4), and node (N0, N1, N2) planes (Fig. 9). Please refer to Fig. 10(a,b) for the plane definitions. Fig. 9 compares the temporal evolutions of v^* and their power spectral density functions between Re = 100 and 300. At $Re = 100$, the v^* signals at the node, middle, and saddle planes exhibit sinusoidal oscillations (Fig. 9a), maintaining a consistent oscillation frequency of $St = 0.117$ (Fig. 9c). Furthermore, the v^* signals at the adjacent node planes demonstrate antiphase behavior, consistent with the observed three-dimensional vortex structures (Fig. 3c). The same holds true for M1 and M2. It implies that the vortex shedding over a half-span is antiphase with that over the other half-span. Conversely, at $Re = 300$, the v^* signals at the three successive node planes exhibit inphase behavior, whereas an antiphase relationship is observed between two neighboring saddle sections. The M1 and M2 signals at the two middle planes within one wavelength are largely inphase due to complex flow interactions between node and saddle planes. Power spectral density functions (Fig. 9d) reveal that the vortex shedding frequency is lower at the node plane ($St_n = 0.16$) than at the saddle plane ($St_s = 0.22$). Because of the difference in the shedding frequencies between the node and saddle planes, the instantaneous phase lag between the signals at the two planes is time-dependent. For example, at instant T1, we observe that N0, N1, N2 and S2 signals are all inphase with each other but antiphase with S1 signal. This suggests that one side of the upper wavelength (N1–N2) exhibits vortex shedding in an inphase manner but the saddle (S1) on the lower wavelength has antiphase vortex shedding with the upper wavelength (Fig. 10a1, a2, c). In other words, the spanwise vortex tube from the lower wavelength (N0 – N1) and the upper wavelength (N1 – N2) exhibit asymmetry, with wavy and nearly straight vortex tubes squarely behind the cylinder, respectively. A contrasting pattern emerges at instant T2, where the positions of wavy and nearly straight vortex tubes reverse (Fig. 10b1, b2, d). The antiphase flow separations at S1 and N0 (or N1, N2) planes at instant T1 gradually transit to the inphase flow at T2. These findings confirm that vortex shedding is antiphase at two adjacent saddle planes for $Re = 300$ but at the two adjacent node planes for $Re = 100$. The difference arises from the steady flow at the saddle planes for Re = 100, facilitating antiphase flow around the two sides of the saddle section. Conversely, at $Re = 300$, the saddle sections have unsteady flow, leading to alternating vortex shedding. Additionally, vortex shedding occurs at one frequency over the entire wavelength at $Re = 100$ but at two distinct frequencies at the node and saddle, respectively, at $Re = 300$, highlighting a complex interplay between the Reynolds number and vortex shedding.

The three-dimensional, time-averaged streamlines are illustrated in Fig. 11, offering a global perspective and a focused view at the *yz*-plane ($x^* = 1.50$). Despite the occurrence of antiphase flow at the adjacent saddle planes, the phenomenon of flow bifurcation in the wake is discernible. The green and red streamlines originating from the bifurcation point spiral towards the saddle and node planes, respectively (Fig. 11a). Furthermore, the pattern of time-averaged streamlines on the *yz*-plane shows a resemblance to that at $Re = 100$, indicating that vortex bifurcation is a consistent feature across the Reynolds numbers ($Re = 100$ and 300). This consistency underscores the inherent nature of vortex bifurcation, irrespective of the Reynolds number.

4. Conclusions

The present study investigates the time-mean streamline patterns and flow topologies of a wavy elliptic cylinder and its wake for $\lambda/D_m = 3.43$, 4.58, and 6.01. The analysis provides valuable insights into flow separation, recirculation bubble behavior, and three-dimensional flow characteristics. By examining the time-mean streamlines on the cylinder surface and wake planes, important flow dynamics associated with the different flow patterns are revealed. The results show that the flow close to the cylinder surface heads for the saddle plane, leading to a delayed flow separation at the saddle compared to the node. This observation emphasizes that the near-surface flow direction plays a crucial role in determining the flow separation. The streamwise size of the

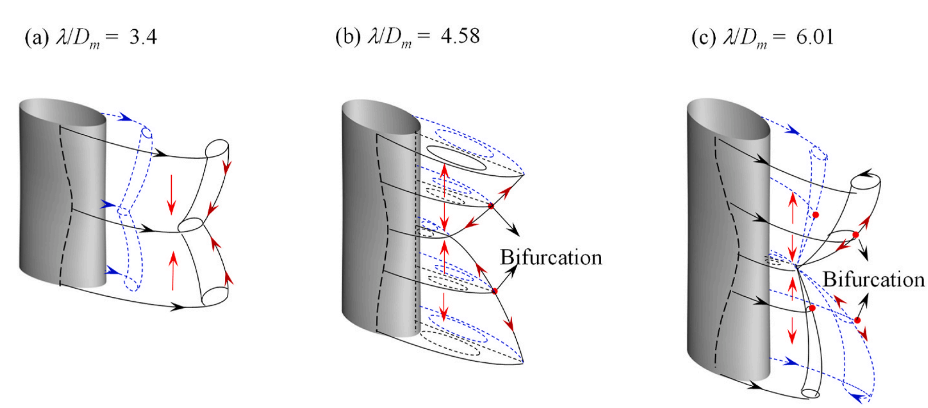

Fig. 8. Overview of three-dimensional flow topology for (a) $\lambda/D_m = 3.43$, (b) $\lambda/D_m = 4.58$, and (c) $\lambda/D_m = 6.01$. Red dots indicate bifurcations in the vortex shedding. Black-solid and blue-dashed lines refer to the streamlines on the left and right sides. Here, $Re = 100$.

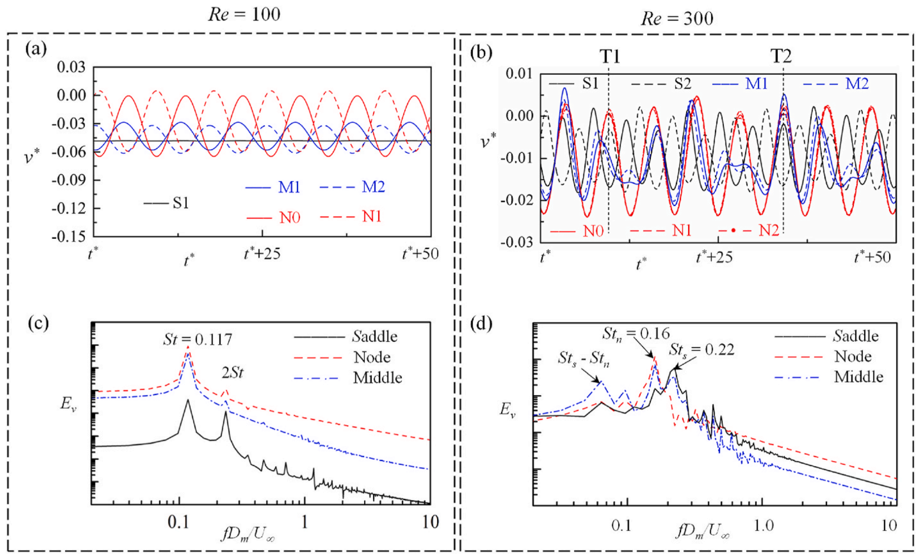

Fig. 9. Time histories (a, c) and power spectral density functions (b, d) of the lateral velocity v^* sampled at $(x^*, y^*) = (3, 1)$ for $\lambda/D_m = 6.01$ (flow pattern IV). (a, c) $Re = 100$; (b, d) $Re = 300$.

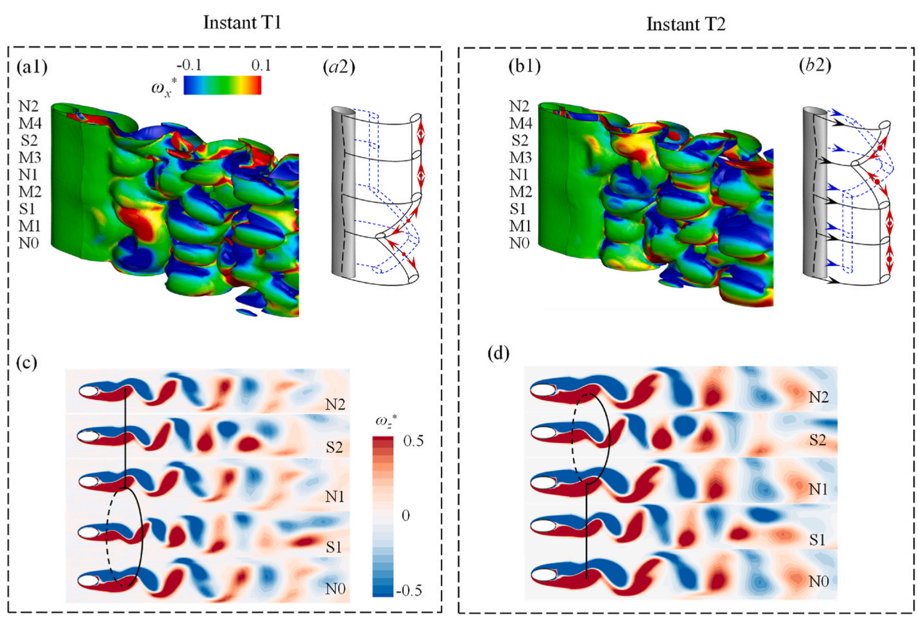

Fig. 10. Instantaneous vortex structures at (a1, a2, c) instants T1 and (b1, b2, d) T2. The upper row displays the (a1, b1) spanwise vorticity (ω_z^*) iso-surface of $\omega_z^* = 0.2$ (colored by streamwise vorticity ω_x^*) and (a2, b2) corresponding vortex shedding sketch. The lower row (c, d) provides the ω_z^* contours at node and saddle sections. In the sketches, the red dots indicate bifurcations in the vortex shedding. Black-solid and blue-dashed lines refer to the streamlines on the left and right sides. Here, $\lambda/D_m = 6.01$, $Re = 300$.

recirculation bubble varies along the cylinder span. The bubble size at the saddle is smaller than that at the node.

The three-dimensional flow topologies associated with the different flow patterns are visualized through time-mean streamlines. The flow at $\lambda/D_m = 3.43$ generates a spiral flow from the node to the saddle in the wake, resulting in counter-rotating vortices and a wavy vortex structure. On the other hand, the flow at $\lambda/D_m = 4.58$ has a stable recirculation bubble that bifurcates at $0.30\lambda/D_m$ away from the saddle plane, engendering spiral flows heading for the saddle and node planes. The flow at $\lambda/D_m = 6.01$ is characterized by antiphase vortex shedding from the two half spans of one wavelength. Again, the flow associated with vortex shedding in a half-span bifurcates, generating spiral flows towards the node and saddle planes, respectively. The bifurcation occurs at $0.38\lambda/D_m$ away from the saddle plane. Overall, the investigation of time-mean streamline patterns, recirculation bubble behavior, and three-dimensional flow topologies provides valuable insights into the complex flow physics around wavy elliptic cylinders. These findings contribute to a deeper understanding of flow separation, vortex shedding, and wake formation. The knowledge gained from this study has broader implications for various engineering applications, including aerodynamics, hydrodynamics, and wind energy.

Vortex bifurcation is further observed at $Re = 300$, which juxtaposes the findings at $Re = 100$. The occurrence of vortex bifurcation, regardless of Re, highlights the wavelength effect on the flow structure in view of the vortex shedding phase and wake stability. This insight is crucial for predicting the aerodynamic and hydrodynamic performance of bluff bodies with similar geometric features. This work offers potential pathways for optimizing designs to achieve desired flow characteristics,

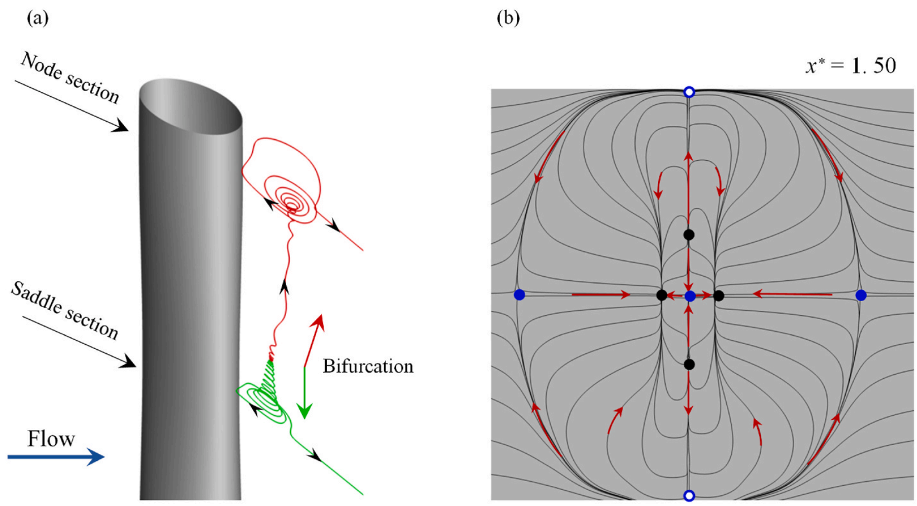

Fig. 11. (a) Three-dimensional time-mean streamlines. (b) Distributions of time-mean streamlines on the *yz*-plane at $x^* = 1.50$. The marks ● and ● denote critical node and saddle points, respectively, while ○ refers to half critical saddle points. Here, $\lambda/D_m = 6.01$, $Re = 300$.

such as reduced drag, enhanced energy efficiency, or controlled vortex-induced vibrations.

CRediT authorship contribution statement

Xiaoyu Shi: Writing – review & editing, Writing – original draft, Validation, Methodology, Investigation, Formal analysis, Data curation. **Md. Mahbub Alam:** Writing – review & editing, Writing – original draft, Validation, Supervision, Software, Resources, Project administration, Investigation, Funding acquisition, Formal analysis, Data curation, Conceptualization. **Hongjun Zhu:** Writing – review & editing. **Chun-ning Ji:** Writing – review & editing. **Honglei Bai:** Writing – review & editing. **Mohsen Sharifpur:** Writing – review & editing.

Declaration of competing interest

The authors declare that they have no known competing financial interests or personal relationships that could have appeared to influence the work reported in this paper.

Data availability

Data will be made available on request.

Acknowledgement

Alam MM wishes to acknowledge support given to them from NSFC through grant 11672096 and from the Khalifa University of Science and Technology through Grants CIRA-2020-057.

References

Abdelhamid, T., Alam, M.M., Islam, M., 2021. Heat transfer and flow around cylinder: effect of corner radius and Reynolds number. Int. J. Heat Mass Transf. 171 (1), 121105.
Ahmed, A., Bays-Muchmore, B., 1992. Transverse flow over a wavy cylinder. Phys. Fluids A: Fluid Dynamics 4 (9), 1959–1967.
Alam, M.M., 2021. Effects of mass and damping on flow-induced vibration of a cylinder interacting with the wake of another cylinder at high reduced velocities. Energies 14 (16), 5148.
Alam, M.M., 2022. A review of cylinder corner effect on flow and heat transfer. J. Wind Eng. Ind. Aerod. 229, 105132.
Alam, M.M., 2023a. Fluctuating forces on bluff bodies and their relationships with flow structures. Ocean Eng 273, 113870.
Alam, M.M., 2023b. Optimum spacing for maximum heat transfer density in tube bundle. Phys. Fluids 35, 093612.
Alam, M.M., Bai, H.L., Zhou, Y., 2016. The wake of two staggered square cylinders. J. Fluid Mech. 801, 475–507.
Alam, M.M., Moriya, M., Takai, K., Sakamoto, H., 2003. Fluctuating fluid forces acting on two circular cylinders in a tandem arrangement at a subcritical Reynolds number. J. Wind Eng. Ind. Aerod. 91, 139–154.
Alam, M.M., 2014. The aerodynamics of a cylinder submerged in the wake of another. J. Fluid Struct. 51, 393–400.
Assi, G., Bearman, P.W., 2018. Vortex-induced vibration of a wavy elliptic cylinder. J. Fluids Struct. 80, 1–21.
Bai, H.L., Alam, M.M., 2018. Dependence of square cylinder wake on Reynolds number. Phys. Fluids 30 (1), 015102.
Bearman, P.W., Owen, J.C., 1998. Reduction of bluff-body drag and suppression of vortex shedding by the introduction of wavy separation lines. J. Fluids Struct. 12, 123–130.
Beem, H.R., Triantafyllou, M.S., 2015. Wake-induced 'slaloming' response explains exquisite sensitivity of seal whisker-like sensors. J. Fluid Mech. 789, 306–322.
Bhatt, R., Alam, M.M., 2018. Vibrations of a square cylinder submerged in a wake. J. Fluid Mech. 853, 301–332.
Cao, Y., Tamura, T., Zhou, D., Bao, Y., Han, Z., 2022. Topological description of near-wall flow around a surface-mounted square cylinder at high Reynolds numbers. J. Fluid Mech. 933, A39.
Castro, I., Kim, J., Stroh, A., Lim, H., 2021. Channel flow with large longitudinal ribs. J. Fluid Mech. 915, A92.
Chen, W., Alam, M.M., Li, Y., Ji, C., 2023. Two-degree-of-freedom flow-induced vibrations of a D-section prism. J. Fluid Mech. 971, A5.
Chen, W., Ji, C., Alam, M.M., Xu, D., An, H., Tong, F., Zhao, Y., 2022. Flow-induced vibrations of a D-section prism at a low Reynolds number. J. Fluid Mech. 941. A52-1-51.
Délery, J.M., 2001. Robert legender and henri werlé: toward the elucidation of three-dimensional separation. Annu. Rev. Fluid Mech. 33, 129–154.
Derakhshandeh, J.F., Alam, M.M., 2019. A review of bluff body wakes. Ocean Eng 182, 475–488.
He, J.W., Glowinski, R., Metcalfe, R., Nordlander, A., Periaux, J., 2000. Active control and drag optimization for flow past a circular cylinder: I. Oscillatory cylinder rotation. J. Comput. Phys. 100, 204501.
Huang, R.F., Chen, J.M., Hsu, C., 2006. Modulation of surface flow and vortex shedding of a circular cylinder in the subcritical regime by a self-excited vibrating rod. J. Fluid Mech. 555, 321–352.
Huang, R.F., Lin, B.N., Yen, S.C., 2010. Time-averaged topological flow patterns and their influence on vortex shedding of a square cylinder in crossflow at incidence. J. Fluid Struct. 26 (3), 406–429.
Hunt, J.C.R., Abell, C.J., Peterka, J.A., Woo, H., 1978. Kinematical studies of the flows around free or surface-mounted obstacles; applying topology to flow visualization. J. Fluid Mech. 86, 179–200.
Jie, H., Liu, Y.Z., 2017. Large eddy simulation and proper orthogonal decomposition of turbulent flow around a vibrissa-shaped cylinder. Intl. J. Heat Fluid Flow 67, 261–277.
Kang, S., 2003. Characteristics of flow over two circular cylinders in a side-by-side arrangement at low Reynolds numbers. Phys. Fluids 15, 2486–2498.
Kumar, D., Mittal, M., Sen, S., 2018. Modification of response and suppression of vortex-shedding in vortex-induced vibrations of an elliptic cylinder. Intl. J. Heat Fluid Flow 71, 406–419.
Lam, K., Lin, Y.F., 2008. Large eddy simulation of flow around wavy cylinders at a subcritical Reynolds number. Int. J. Heat Fluid Flow 29, 1071–1088.
Lam, K., Lin, Y.F., 2009. Effects of wavelength and amplitude of a wavy cylinder in cross-flow at low Reynolds numbers. J. Fluid Mech. 620, 195–220.
Le Clainche, S., Rodriguez, D., Theofilis, V., Soria, J., 2016. Formation of three-dimensional structures in the hemisphere-cylinder. AIAA J. 54 (12), 1–11.

Liakos, A., Malamataris, N.A., 2014. Direct numerical simulation of steady state, three dimensional, laminar flow around a wall mounted cube. Phys. Fluids 26 (5), 053603.
Liakos, A., Malamataris, N.A., 2016. Three-dimensional, laminar flow past a short, surface mounted cylinder. AIAA J. 2310–2321.
Lin, Y.F., Bai, H.L., Alam, M.M., Zhang, W.G., Lam, K., 2016. Effects of large spanwise wavelength on the wake of a sinusoidal wavy cylinder. J. Fluids Struct. 61, 392–409.
Mondal, M., Alam, M.M., 2023. Blockage effect on wakes of various bluff bodies: a review of confined flow. Ocean Eng 268, 115592.
Paul, I., Prakash, K.A., Vengadesan, S., Pulletikurthi, V., 2016. Analysis and characterization of momentum and thermal wakes of elliptic cylinders. J. Fluid Mech. 807, 303–323.
Qin, B., Alam, M.M., Zhou, Y., 2017. Two tandem cylinders of different diameters in crossflow: flow-induced vibration. J. Fluid Mech. 829, 621–658.
Qin, B., Alam, M.M., Zhou, Y., 2019. Free vibrations of two tandem elastically mounted cylinders in cross flow. J. Fluid Mech. 861, 349–381.
Rastan, M.R., Alam, M.M., Zhu, H., Ji, C., 2022. Onset of vortex shedding from a bluff body modified from square cylinder. Ocean Eng 244, 110393.
Rastan, M.R., Sohankar, A., Alam, M.M., 2021. Flow and heat transfer across two inline rotating cylinders: effects of blockage, gap spacing, Reynolds number, and rotation direction. Int.l J. Heat Mass Tran. 174, 121324.
Rinehart, A., Shyam, V., Zhang, W., 2017. Characterization of seal whisker morphology: implications for whisker-inspired flow control applications. Bioinspir. Biomim. 12, 066005.
Shi, X., Alam, M., Bai, H., 2020. Wakes of elliptical cylinders at low Reynolds number. Int. J. Heat Fluid Flow 82, 108553.
Shi, X., Bai, H., Alam, M.M., Ji, C., Zhu, H., 2023. Wake of wavy elliptic cylinder at a low Reynolds number: wavelength effect. J. Fluid Mech. 969, A22.
Stroh, A., Hasegawa, Y., Kriegseis, J., Frohnapfel, B., 2016. Secondary vortices over surfaces with spanwise varying drag. J. Turbul. 17 (12), 1142–1158.
Thompson, M.C., Radi, A., Rao, A., Sheridan, J., Hourigan, K., 2014. Low-Reynolds-number wakes of elliptical cylinders: from the circular cylinder to the normal flat plate. J. Fluid Mech. 751, 570–600.
Wang, L., Alam, M.M., Zhou, Y., 2017. Two tandem cylinders of different diameters in cross-flow: effect of an upstream cylinder on wake dynamics. J. Fluid Mech. 836, 5–42.
Wang, S., Liu, Y., 2016. Wake dynamics behinds a seal-vibrissa-shaped cylinder: a comparative study by time-resolved particle velocimetry measurements. Exp. Fluids 57, 32.
Williamson, C.H.K., 1989. Oblique and parallel modes of vortex shedding in the wake of a circular cylinder at low Reynolds numbers. J. Fluid Mech. 206, 579–627.
Williamson, C.H.K., 1996. Vortex dynamics in the cylinder wake. Annu. Rev. Fluid Mech. 28, 477–539.
Zhang, H.Q., Fey, U., Noack, B.R., Konig, M., Eckelmann, H., 1995. On the transition of the cylinder wake. Phys. Fluids 7 (4), 779–794.
Zheng, Q., Alam, M.M., 2017. Intrinsic features of flow past three square prisms in side-by-side arrangement. J. Fluid Mech. 826, 996–1033.
Zheng, Q., Alam, M.M., 2019. Evolution of the wake of three inline square prisms. Phys. Rev. Fluids 4 (10), 104701, 1-35.